Automated image analysis system for renal filtration barrier integrity of potassium bromate treated adult male albino rat

Automated based Image Analysis System for Renal Filtration Barrier Integrity of Potassium Bromate Treated Adult Male Albino Rat

Shaima Mostafa Ibrahim Kashef[1], Amal Ali Ahmed Abd El Hafez[1], Naglaa Ibrahim Sarhan[1], AWatif Omar El-Shal[1], Mohamed Maher Ata[2], Amira S. Ashour[3,*], Nilanjan Dey[4], Mustafa M. Abd Elnaby[3], R. Simon Sherratt[5]

[1]Department of Histology Department, Faculty of Medicine, Tanta University, Egypt

[2]MISR Higher Institute for Engineering & Technology, Mansoura, Egypt

[3]Department of Electronics and Electrical Communication Engineering, Faculty of Engineering, Tanta University, Egypt

[4]Department of Information Technology, Techno India College of Technology, Rajarhat, India

[5]Department of Biomedical Engineering, University of Reading, RG6 6AY, UK

Corresponding author: Amira S. Ashour

Email: amirasashour@yahoo.com

Abstract

Potassium bromate ($KBrO_3$) is a potent nephrotoxic agent that leads to a significant decrease in the activities of renal antioxidant capacity, antioxidant loss and restoration of the renal dysfunction. Several measurements are used to examine the kidney status, including the base width of the foot, the slit pore diameter, and the glomerular basement membrane thickness of the kidney. In this work, morphometric analysis based on image processing is carried out to assess the filtration barrier integrity parameters, which indicates the degree of recovery against the nephrotoxic effect of the $KBrO_3$ on the renal cortex of adult male albino rat and assesses the capability of the renal cortex to recover after its cessation. The morphometric methods based proposed image analysis system enabled the identification of the renal status of different groups, namely the control, potassium bromate affected, and the recovered groups, according to the variation of the measured parameters is a powerful tool. The proposed image analysis system provided a radical geometric morphometrics, which includes morphological operations and structuring element processes in order to identify the glomerular filtration barrier and the feet for further measurements in each case study. The results established that the average lengths of the feet in the histological microscopic images are 465.2397 nm, 278.189 nm, and 393.2347 nm for the control, $KBrO_3$ affected rats and the recovered rats; respectively.

Keywords: Potassium bromate, glomerular filtration barrier, renal recovery, morphometrics, morphological operations, Euclidean distance

1. Introduction

Potassium bromate (KBrO3) is broadly considered as food additive and flour improver [1]. However, it possesses the potential of inducing kidney failure, deafness, and testicular mesothelial cancers in rats. Additionally, the KBrO3 has microscopic nephrotoxic effect after both short-/ long- term exposures to sub-lethal dose in Wistar rats [2, 3]. Consequently, different measurements are required to examine the kidney status. Such measurements of the microscopic histological samples from the kidney include the base width of the foot, the slit pore diameter, and the glomerular basement membrane thickness of the kidney. Typically, the mammalian species' kidney has a bean-shaped appearance, where the kidney's functional unit is called nephron that comprises of proximal convoluted tubules, corpuscle, distal convoluted tubules, loop of Henle, and collecting tubules [4]. The histology and morphology studies of the Albino rat's kidney are beneficial in physiological and pathological research [5]. Histological procedures have a promising role for detecting pathological disease mechanisms in tissue slices acquired from experimental animal models or renal biopsies. Precise histopathology quantification is essential for disease progression evaluation and for defining the therapeutic strategies efficiency [6]. Several studies have been conducted based on semi-quantitative recording methods that may subject to scoring bias and suffer from the lack of sensitivity. Accordingly, more sophisticated, sensitive and reliable procedures become essential. Applying digital imaging techniques to the microscopic findings offers precise histological assessment. Traditional multivariate morphometrics for shape and size variation have effectively distinguished control groups from diseased ones. Nevertheless, the traditional procedures have been enriched by image processing methods through superior data collection, innovative analytical tools and more active shape descriptors [7].

Accurate quantification of the pathological kidney microscopic samples can be performed using different image analysis techniques. Computer aided diagnosis (CAD) has an imperative role in histopathological imaging. Different image processing methods have been used for image texture classification, nuclei and gland segmentation, cells identification and counting to derive assessable measurements of the disease characteristics and the different grades of certain disease. Demir and Yener [8] proposed analysis approaches in the cell/tissue levels for cancer diagnosis using histopathology image processing methods. Feature extraction, morphological processing, and thresholding techniques have been employed. On neuroblastoma histopathological images, Sertel *et al.* [9] suggested a likelihood function estimation based image analysis technique. The results detected cancer cells with 81.1% sensitivity using component-wise-2 step thresholding. Kayser *et al*. [10] separated the object space and the background using thresholding methods. Texture analysis was also measured to classify the different objects. Rangan and Tesch [11] applied image scaling, object thickness and size assessment, point counting, cell counting and area stained calibration measurements using image analysis tools using the ImageJ software. In order to detect and identify particular structures, the threshold levels were adjusted while observing the histogram of the image to evaluate the accumulation of inflammatory cells, and the glomerular hypertrophy.

In this work, a proposed automated image analysis procedure is applied to assess the renal histopathology. The main contribution of the present work is to develop an automated

segmentation method to detect the feet, the pores (gaps), and the glomerular basement membrane of the kidney in the complicated microscopic pathological images. A thresholding technique is used to determine the area of interest in the different cases, namely the control, affected by KBrO3, and the recovered for further analysis and measurements. The segmentation based on thresholding is applied for the identification of the different structures separation from the background area.

The organization of the further coming sections is as follows. Section 2 highlights the histological experiment and the used dataset along with the methodology of the proposed image processing method. Section 3 includes the results with discussion, which is followed by the conclusions in Section 4.

2. Methodology and Proposed System

2.1. Dataset

This work was carried out on 15 adult male albino rats divided into three equal groups, namely i) Group-A: control group for studying the histological structure of the normal renal tissue, ii) Group-B: affected by KBrO3, where the albino rats received 20 mg/kg/dose of KBrO3 by intraperitoneal injection twice per week for four weeks, and iii) group-C: recovered group. Finally, the animals were sacrificed and their kidneys were processed for electron microscope and quantitative analysis. This experiment was done in the EM Unit of Faculty of Medicine, Tanta University, Egypt on TEM images to investigate the foot length, the base width of the foot, and the slit pore (gaps) width in the glomerular basement membrane in each group.

2.2. Computer Vision based Approaches

A computer vision based approach is proposed for estimating the average width of the gaps between the feet as well as the average thickness for the three groups, namely controlled based microscopic images, potassium based images and the recovery based images. To identify the regions of interest, objects separation from the background through segmentation processes is essential [12]. Initially, the appropriate test images are preprocessed using the median filter in order to obtain more convenient images for further analysis. In addition, the original images are transformed into gray scale in order to represent each pixel in 8 bit per pixel format. This format would be the most convenient in order to decrease the processing time. Afterwards, image binarization is executed to represent a smoothing algorithm by creating a morphological non-flat structuring element. Assume that A refers to the binary image and B is the structuring element, thus, the dilation of A by B would be performed by reflecting B about its origin and shifting the reflected version by z as follows:

$$A \oplus B = \left\{ Z \middle| (\hat{B})z \cap A \neq \emptyset \right\} \quad (1)$$

This dilation process is considered a set of all displacements z, where $\hat{B}$ and A overlap by one element at least. Therefore, equation (1) can be modified as:

$$A \oplus B = \left\{ Z \middle| [(\hat{B})z \cap A] \subset A \right\} \quad (2)$$

Moreover, erosion is used for shrinking element *A* by using element *B* according to the following expression:

$$A \ominus B = \left\{ Z \middle| [(\hat{B})z \subseteq A \right\} \tag{3}$$

The erosion of *A* by *B* consists of a set of points *z* at which *B* is translated by *z* will be combined in *A*. Furthermore, in order to obtain completely filled feet, a filling holes methodology has been performed. The filling procedure has been manipulated according to the following expression:

$$X_k = (X_{k-1} \oplus B) \cap A^c \tag{4}$$

After the filling process, extraction of the connected components is performed by selecting a point on a binary object *A*. This acts as the region filling process, but with the use of the conjunction the object *A* instead of its complement. In the two-dimensional (2D) image, the connected components are in the form of clusters of pixels with the same value, which are connected to each other through either 4-pixel, or 8-pixel connectivity. The 4-pixel connectivity would group all pixels that contact each other on any of their four faces, while the 8-pixel would group pixels that are connected along any face or corner. This can be represented as follows:

$$X_k = (X_{k-1} \oplus B) \cap A \tag{5}$$

Consequently, all feet are segmented correctly and the distance estimation is performed using the Euclidean distance. The Euclidean distance is calculated using the Euclidean norm according to Figure 1.

0	0	0
0	1	0
0	0	0
image		

1.41	1.0	1.41
1.0	0.0	1.0
1.41	1.0	1.41
Distance Transform		

Figure 1. Euclidean distance of an image.

In the two dimensional (2D) Euclidean spaces, consider any two points P and Q having (p_1, p_2) and (q_1, q_2) coordinates, respectively. The distance between the p and q points can be defined as the square root of the sum of the squares of the differences between their consistent coordinates.The Euclidean distance in the 2D Euclidean geometry between points $a = (a_x, a_y)$ and $b = (b_x, b_y)$ can be given by:

$$d(a,b) = f\overline{(b_x - a_x)^2 + (b_y - a_y)^2} \tag{6}$$

The pseudo-code of the proposed approach to measure feet length can be summarized as presented in Algorithm 1.

Algorithm 1: Proposed approach for feet length measurements

Start

Stage1: Image reading

Read input microscopic image X

Construct the image gray scaled matrix Y

Stage2: Image smoothing

Create a morphological non flat Structuring Element (SE)

Dilate image using Z=y*SE

Stage 3: Image binarization

Apply the image thresholding procedure

Create the image complement

Fill the holes, where *t*= predefined threshold

Remove all connected components less than *t*

Isolate the feet as disconnected blobs

Determine the position for the region of interest

Express the region by 8 connected components

Crop each feet with the appropriate in-between gaps of interest

Stage 4: Euclidean distance estimation

Load the column vector *x*

Initialize the minimum distance to the first element of c_b, i.e. set id_x=1;

C***alculate*** the distance by normalized values of (x-c_b) for all c_b;

If d < distance set

distance = d;

Put id_x=index;

Endif

Stop

In Algorithm 1, the SE has an ellipsoid ball shape of radius R=5 and height H=5. In order to measure the width of the gaps between each pair of feet, the proposed mask is used to remove from binary image all the small objects, where all are connected objects having fewer than P pixels (in the present analysis p=100000). This operation is known as area opening. In the present work, a connectivity of 8 connected neighborhoods was applied. However, any connectivity can be used using following scalar values: i) Connectivity of 4, means two-dimensional four-connected neighborhood, ii) Connectivity of 8, means two-dimensional eight-connected neighborhood, iii) Connectivity of 6, means three-dimensional six-connected neighborhood, iv) Connectivity of 18, means three-dimensional 18-connected neighborhood, and v) Connectivity of 26, means three-dimensional 26-connected neighborhood. The distance was estimated using the Euclidean distance between two specified points. For feet, by applying edge detection techniques (Sobel technique), the centroid of the upper and lower edges (midpoint of upper and lower edged) was specified, and then the estimated distance was calculated to measure the gap width using the same criteria.

2.3. Proposed System

In the present work, in order to study the potassium bromate effect on the malpighian corpuscles of the adult male albino rat, an image processing procedure is proposed to analyze the electronic microscope images based morphometric processes. Consequently, for the three cases (groups), the proposed system is applied as illustrated in Figure 2.

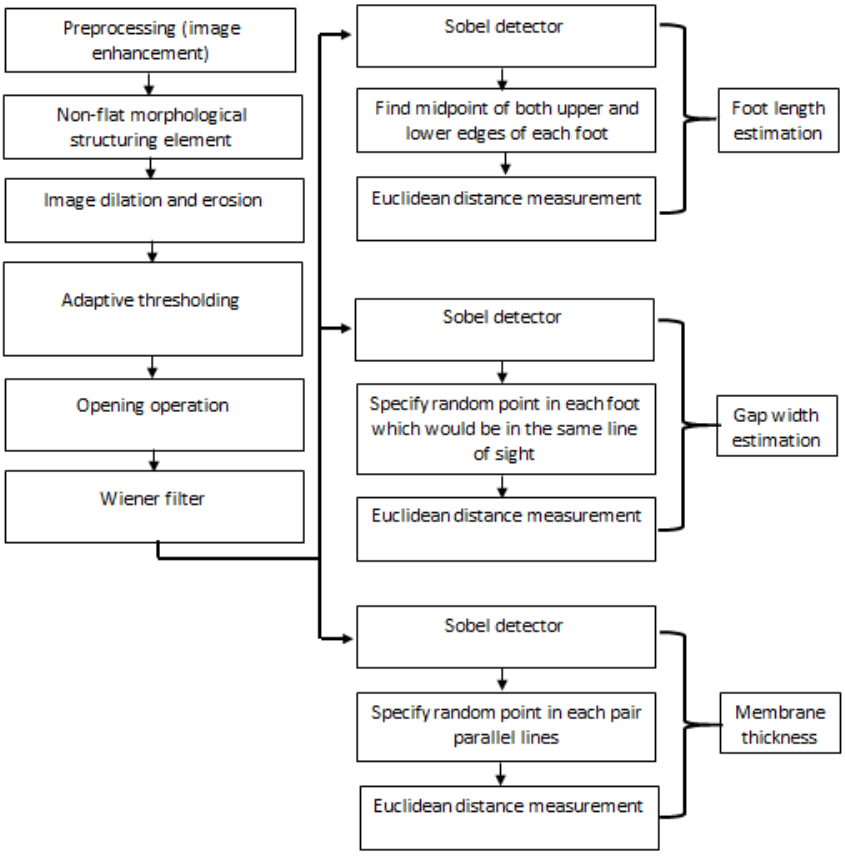

Figure 2. Proposed system block diagram.

Figure 2 illustrates that the histological microscopic images were enhanced and pre-processed using a median filter after which an ellipsoid structuring element was used as a non-flat morphological operation. In order to perform image filling, dilation and erosion operations were performed. In order to perform image filling, dilation and erosion operations were carried out followed by adaptive thresholding using Otsu's method [13-15]. Otsu's method maximizes the "between class variance" of the segmented classes by minimizing the "within class variance" of the segmented classes. In the current study, a modified Otsu's algorithm was deployed by using three interval intensities instead of two intervals which significantly improves the accuracy of thresholding criteria due to its ability of dealing with discontinuous gray images with high intensity variation.

Moreover, an area opening operation was performed in order to remove the small connected objects. Then, the wiener filter was applied to smooth the resultant binary image. Finally, an edge detection-based detector was applied. At each point in the region of interest, the Sobel edge

detector was used to define the approximate absolute gradient amplitude. The Sobel detector emphasizes the regions of high spatial frequencies that correspond to edges. In addition, its larger convolution kernel leads to more smooth images, which makes Sobel operator less sensitive to noise. The Sobel operator also produces higher output vales for similar edges compared to the other detectors, such as the Canny detector. Consequently, in the present work, a Sobel edge detector was applied in order to detect the regions of interest, computed in a parallel process. In this step, the Sobel edge detector was executed three times in parallel to determine each of the following regions separately, being the feet, the gaps, and the membrane.

Figure 2 presents that after detecting the required regions, the filtration barrier integrity parameters were measured as follows: i) the feet length was estimated by finding the midpoint of both the upper and lower edges of each foot, where the Euclidean distance was calculated between the two points, ii) the lengths (widths) of each gap between any two succeeding feet were estimated by specifying a random point in each foot which would be in the same line of sight for further measuring the Euclidean distance between each two points, which indicates each gap width, and iii) the membrane thickness was determined by specifying random point in each pair of the membrane parallel lines and measure the Euclidean distance between each two points.

3. Experimental Results and Discussion

3.1. Dataset

Ultrathin sections of control kidney at the filtration barrier were formed of glomerular basement membrane (GBM), fenestrated endothelium and podocyte foot processes separated by filtration slits. The GBM appeared regular and continuous with outer and inner electrolucent layers and intermediate electrodense layer in the control group. The KBrO3 induced massive diffuse histological alterations involving all components of renal corpuscles including shortening and broadening of the minor foot processes, widening of the capillary fenesterae and absence of slit diaphragm with widening of the spaces between the feet processes. Most of these changes were disappeared after withdrawal of potassium bromate. Figure 3 illustrates the EM samples from each group.

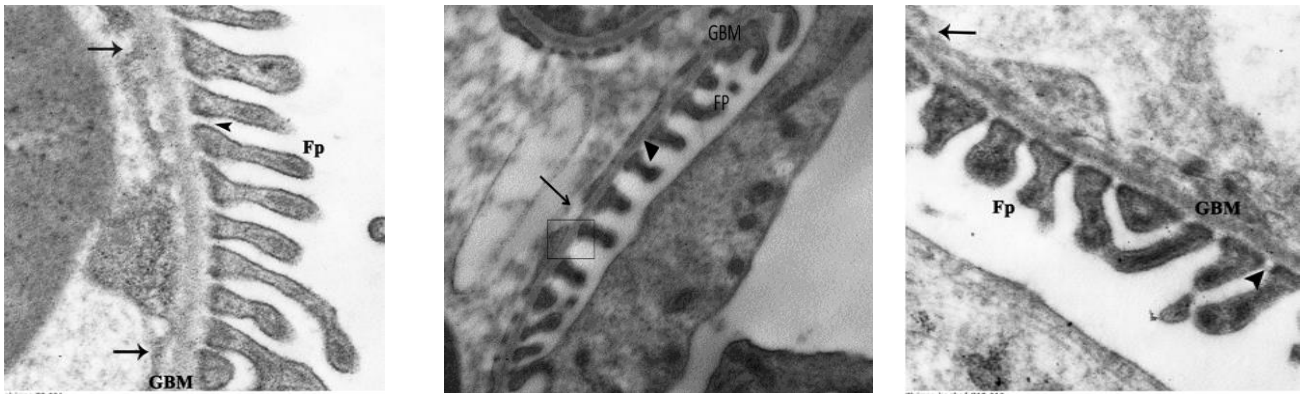

(a) (b) (c)

Figure 3. An electron micrograph (at X15000 magnification) of ultrathin section of renal cortex of the three experimental groups of rats, where (a) control group, (b) potassium affected group, and (c) recovered group.

Figure 3 (a) shows the three components of the filtration barrier in the control group sample, which are namely the GBM, fenestrated endothelium (→), and regular spaced feet processes (Fp) separated by filtration slits that bridged by the slit diaphragm (►). The GBM appears with outer and inner electrolucent layers with intermediate electron dense layer. Figure 3 (b) illustrates shortening and broadening of the minor foot processes (►), widening of the capillary fenesterae (→), and absent slit diaphragm in association with increased the distance between foot processes in the case of the potassium affected group. Figure 3 (c) displays findings similar to the control group. Generally, Figure 3 illustrates that the control experimental group has a well-known histological features of normal renal cortex by the electron microscopes. Glomerular blood capillaries of the affected Malpighian corpuscles show fusion or losing of their fenestrae. The GBM in some areas is obviously thickened and irregular, while in other parts thin or absent GBM exists. All these changes were associated with different sized electron dense granules scattered in the cytoplasm and even shedded into the lumen. The $KBrO_3$ treated group revealed significant increase in the percentage of Malpighian corpuscles with sclerotic and hypercellular glomeruli, proximal tubules damage and numbers of fields displaying mononuclear cellular infiltration when it was compared with the control group. Figure 3 (c) illustrates the recovery group showing also significant increase in all parameters compared to their values in the control group.

3.2. Electronic Microscope Image Processing based Morphometric Study

The main steps of the proposed approach are illustrated in Figure 4, being a) gray scale electronic microscope image, (b) smoothed image using the morphological operations, (c) binarization, (d) dilation and erosion, (e) filling and compensation, (f) segmented image, and (g) feet isolation for measurements as an example.

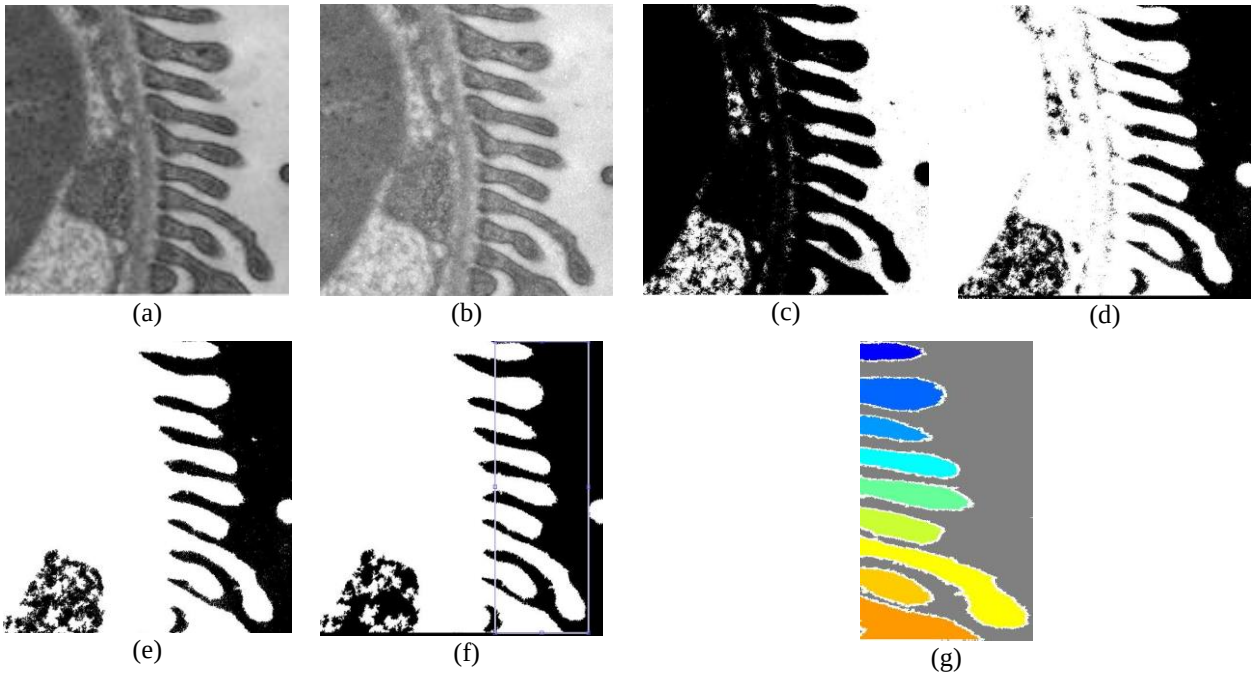

Figure 4. Steps of the proposed approach, (a) gray scale image, (b) Smoothed image, (c) binarized image, (d) dilation and erosion result, (e) filled image, (f) segmented image, and (g) separated feet.

3.2.1. Feet lengths measurements

The proposed approach is applied on the EM images of the three cases from which 49 feet are extracted from the control images, 23 feet from the potassium affected images, and 27 feet from the recovery cases. Figure 5 illustrates the measured feet lengths that exist in a sample image from each case.

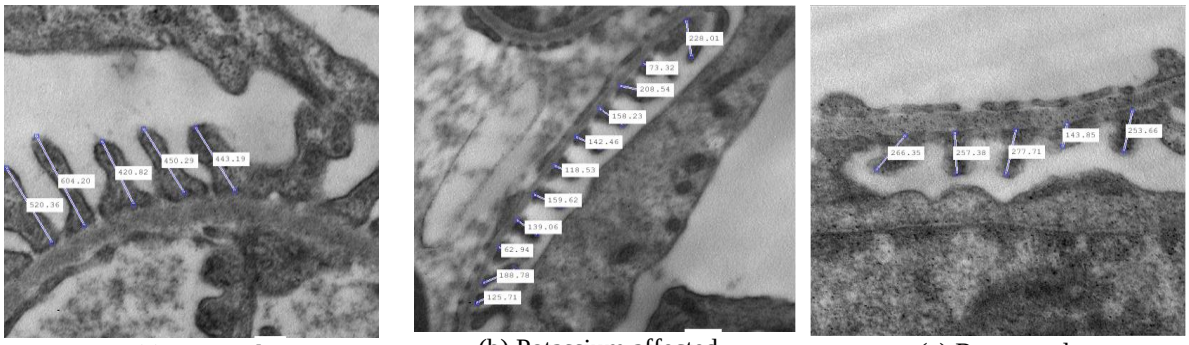

(a) Control (b) Potassium affected (c) Recovered

Figure 5. Foot length measurements on a sample images.

Moreover, in order to display the range of the feet lengths in each case to find a relation and indication from the foot length regarding the case under interest. Figure 6 demonstrates the feet lengths of 5 foots' as samples in an image from the used dataset in each case, namely control, potassium affected, and recovered cases.

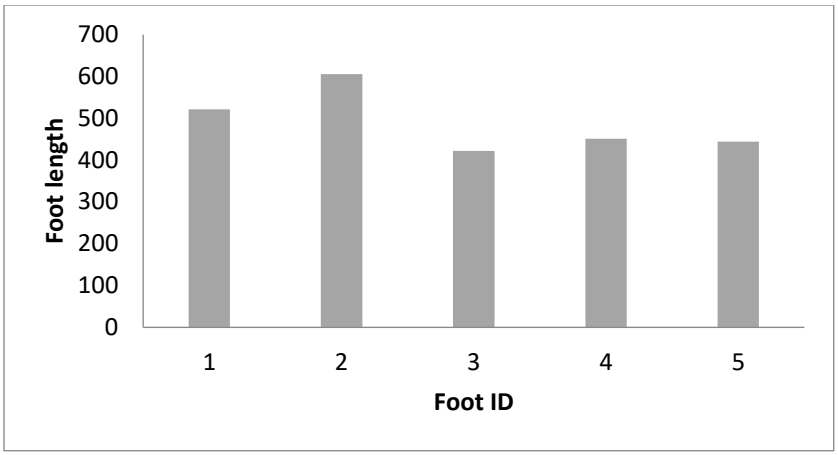

(a)

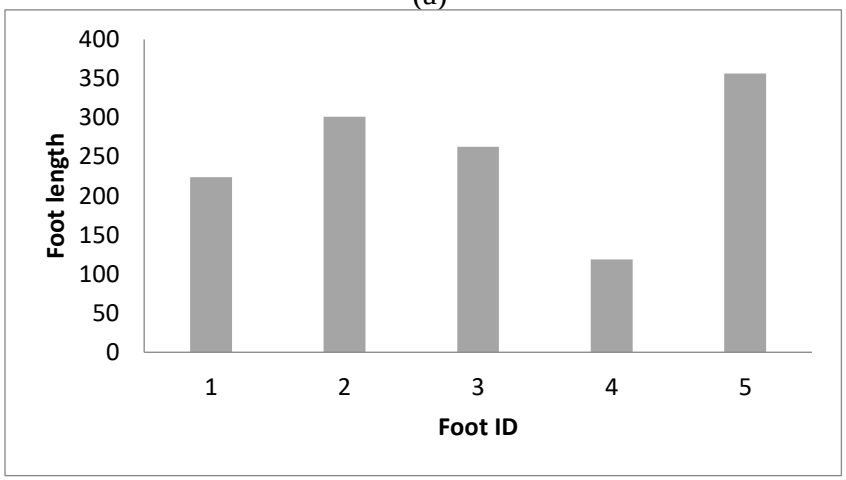

(b)

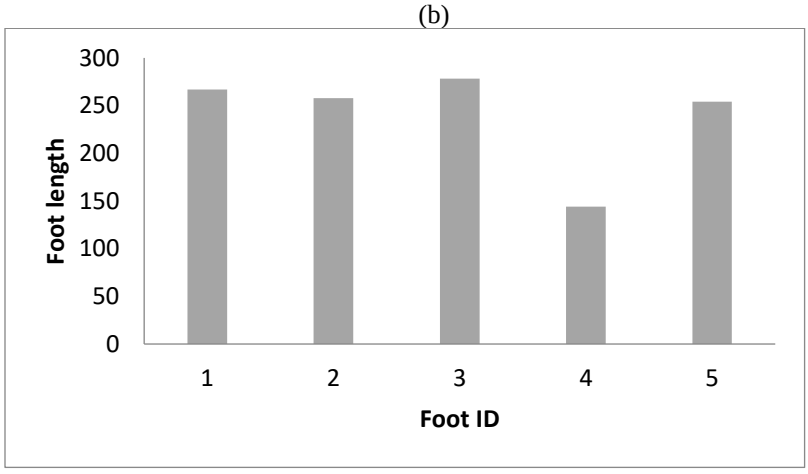

(c)

Figure 6. Feet lengths range in three sample images for the three cases (a) control, (b) potassium affected, and (c) recovered.

Figure 6 illustrates that in both the control and recovered cases, the feet lengths are mostly within the range for 350nm with maximum length of about 900nm and 710 nm; respectively. In addition, the average and standard deviation of the measure are reported in Table 1.

Table 1. Average foot lengths measurements.

Case study	Average foot length (nm)	Standard deviation (nm)
Control images	465.2397	171.0192
Potassium affected images	278.189	96.4127
Recovered images	393.2347	148.2173

The results in Table 1 show a decrease in feet lengths due to the potassium compared to the control and the recovered cases. The decrease in the feet length could be attributed to the loss of cytoskeletal integrity of the podocytes with subsequent destabilization and disruption of the filtration slit membrane which leads to broadening of foot process [16].

3.2.2. Gap width measurements

The proposed approach was applied on the EM images of the three cases from which 43 gaps were extracted from the control images, 23 gaps from the potassium affected images, and 28 gaps from the recovery cases. Figure 7 illustrates the measured gaps width that existed in a sample image from each case.

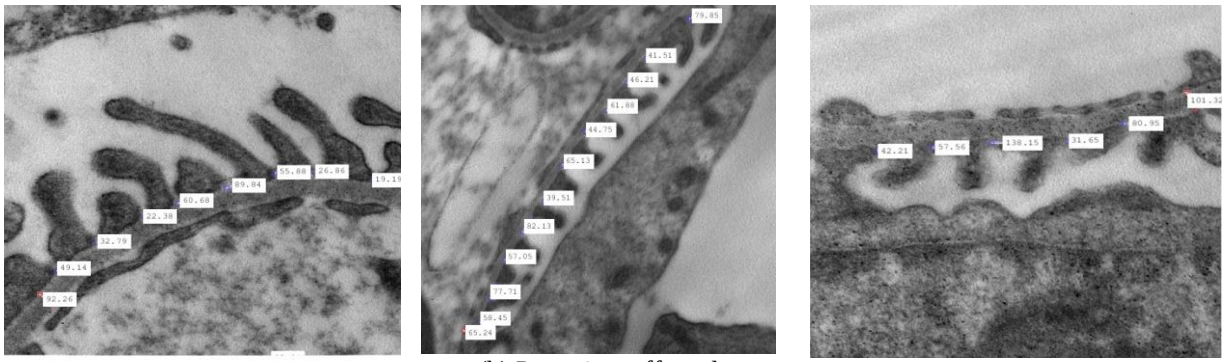

(a) Control (b) Potassium affected (c)Recovered

Figure 7. Gaps width measurements on a sample images.

Moreover, in order to display the range of the gap lengths in each case to find a relationship and indication from the gap length regarding the case under interest. Figure 8 demonstrates the gap widths between 6 feet (5 gaps) as samples in an image from the used dataset in each case, namely control, potassium affected, and recovered cases.

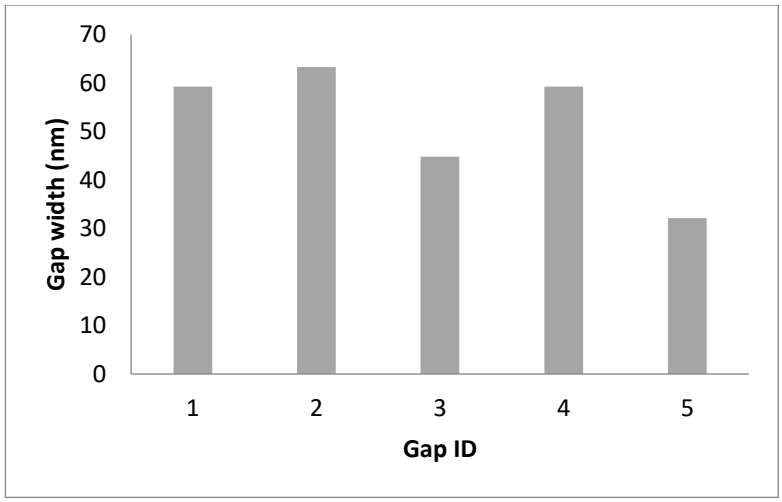

(a)

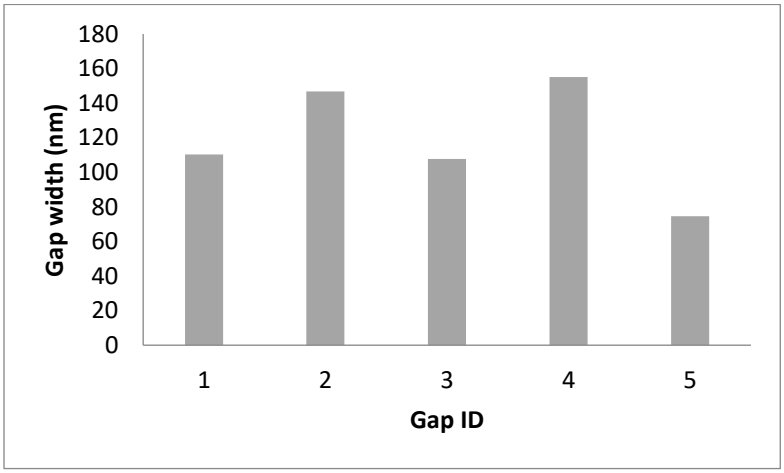

(b)

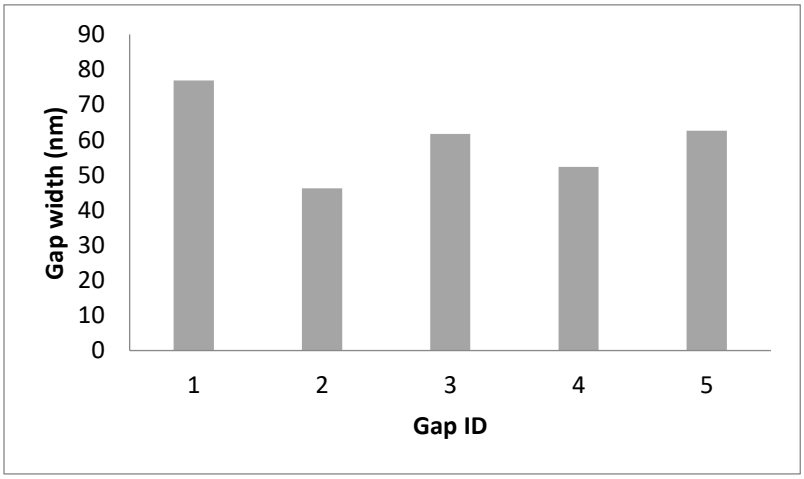

(c)

Figure 8. Gap widths range between 6 feet (5 gaps) as samples in an image for the three cases (a) control, (b) potassium affected, and (c) recovered.

Figure 8 illustrates that in the control and recovered cases, the gap widths are mostly within the range for 20nm to 80 nm, while the gap widths increases in the potassium affected cases. In addition, the average and standard deviation of the measure are reported in Table 2.

Table 2. Average gaps widths measurements.

Case study	Average gap width (nm)	Standard deviation (nm)
Control	41.83635	18.8479
Potassium affected	89.7413	35.7823
Recovered	52.66293	22.5113

Table 2 reveals that the potassium increases the gaps widths compared to the control and the recovered cases.

3.2.3 Membrane thickness measurements

The proposed approach was applied on the EM images of the three cases from which the membranes were extracted in each case. Figure 9 illustrates the extracted membranes that existed in a sample image from each case, which is indicated by a red line.

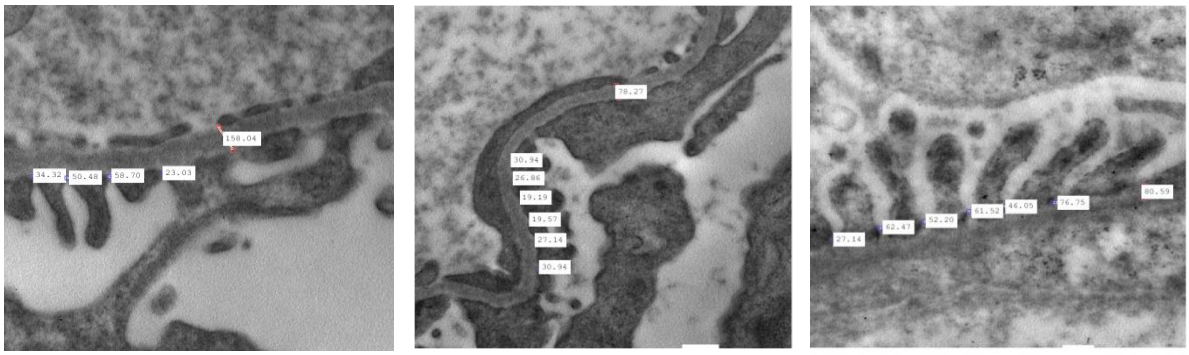

Control (b) Potassium affected (c)Recovered

Figure 9. Membrane thickness measurements on a sample images.

Moreover, in order to display the range of the membranes thickness values in each case to find a relation and indication from the membrane thickness regarding the case under interest, Figure 10 demonstrates the membranes' thickness values in each case for the same image having feet lengths and gap widths in Figures 6 and 8, respectively.

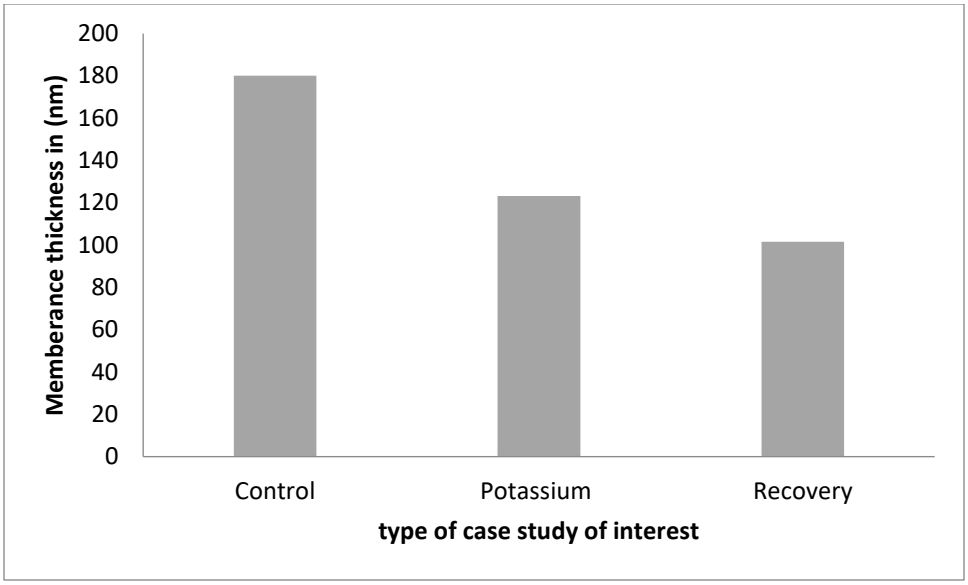

Figure 10. Membrane thickness for an image in each of the three cases, namely (a) control, (b) potassium affected, and (c) recovered.

Figure 10 illustrates that in the control and recovered cases, the membrane thickness were primarily decreased in the potassium affected cases compared to the control cases. In addition, the average and standard deviation of the measure are reported in Table 3.

Table 3. Average membrane thickness measurements

Case study	Average thickness (nm)	Standard deviation (nm)
Controlled	154.552	32.1305
potassium	117.01	34.3064
recovery	110.3008	33.3728

Table 3 reveals that the potassium decreased the membrane thickness compared to the control cases, however, no significant difference was present when compared to the recovered cases. Generally, the increased width of the filtration slits and the decreased thickness of the basement membrane are mostly attributed to the cellular damage induced in the podocytes of potassium bromate treated rats. This cell (podocyte) cooperate with mesangial cells to support the structure and function of the glomerulus and to synthesize matrix molecules to the GBM, including type IV collagen, agrin, entactin and laminin [17]. Several works have demonstrated that KBrO3 produces reactive oxygen species (ROS) as well as DNA damage [18]. Several works have demonstrated that KBrO3 produces reactive oxygen species (ROS) as well as DNA damage [15]. In addition, the obtained control GBM thickness with average value of 154.55 nm is also matched with the corresponding range reported by Succar *et al*. [19]. In this work they reported that the mean thickness is ranging from 50 nm to 165 nm. Figure 11 demonstrates the average and standard deviation of both the gap width and the membrane thickness.

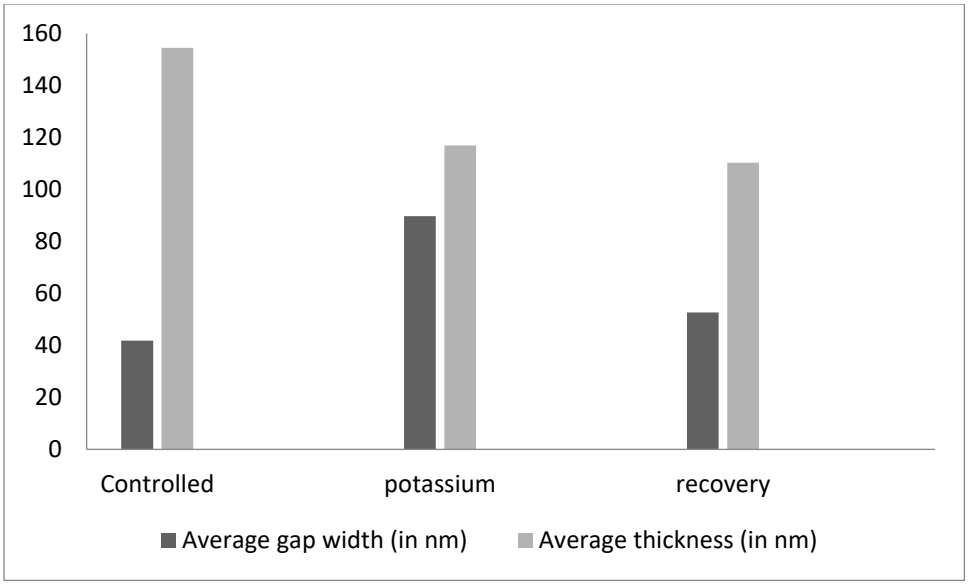

Figure 11. Average gaps width and membrane thickness.

The preceding results established the efficiency of the proposed method to determine and measure the base width of the foot, the slit pore diameter, and the glomerular basement membrane thickness of the kidney in the different cases. Furthermore, it is recommended to include post-processing and correction techniques [20- 22] in the future in order to increase the accuracy of the proposed system. In addition, the proposed method can be generalized by using optimization algorithms to adapt the used set of parameters, such as threshold, connectivity, and SE radius instead of being specific-based case-study to handle several scenarios including luminance, scale or resolution changes.

In the present work, due to the limited size of the used dataset, the evaluation of the proposed methods was carried out by comparing the obtained measurement of base width of the foot, the slit pore diameter, and the glomerular basement membrane thickness of the kidney in the different cases, using our proposed method with the medical records of the same dimensions along with the observation of the medical experts. Furthermore, it is recommended to increase the dimension of the used dataset to validate and evaluate the proposed method using different metrics and measure the accuracy in comparison with other strategies state-of-the-art methods. Then also, these measurements can be used to classify between the different cases using different classification techniques [23- 27].

4. Conclusion

Potassium bromate (KBrO3) affects the functionality of the kidney that may lead to renal failure. For accurate diagnosis of the kidney status, histological microscopic samples can be captured for further microscopic image analysis to measure different parameters to assess the kidney status. These measurements include the base width of the foot, the slit pore diameter, and the glomerular basement membrane thickness of the kidney. The current work proposed an image processing system based on the morphometric analysis to assess the filtration barrier integrity parameters. These measurements are used to evaluate the recovery versus the

nephrotoxic effect of the KBrO3 on the renal cortex of adult male albino rat to identify the renal status at different cases, including the control, potassium bromate affected, and the recovered groups. The proposed image analysis system identified the glomerular filtration barrier and the feet for further measurements in each case study. From the histological microscopic images, the experimental results revealed that the average feet lengths are 465.2397 nm, 278.189 nm, and 393.2347 nm for the control, KBrO3 affected and recovered rats; respectively. Thus, it could be concluded that KBrO3 induced ultrastructural alterations in the components of renal filtration barrier of adult male albino rat. Also, renal tissue has the capacity to recover after cessation of KBrO3.

References

[1] Hassan, I., Husain, F. M., Khan, R. A., Ebaid, H., Al-Tamimi, J., Alhazza, I. M., ... & Ibrahim, K. E. (2019). Ameliorative effect of zinc oxide nanoparticles against potassium bromate-mediated toxicity in Swiss albino rats. *Environmental Science and Pollution Research*, *26*(10), 9966-9980.

[2] Ahmad, M. K., Naqshbandi, A., Fareed, M., & Mahmood, R. (2012). Oral administration of a nephrotoxic dose of potassium bromate, a food additive, alters renal redox and metabolic status and inhibits brush border membrane enzymes in rats. *Food chemistry*, *134*(2), 980-985.

[3] Dimkpa, D., Ukoha, U. U., Udemezue, O. O., Okafor, J. I., Ufondu, O. A., & Anyiam, D. C. (2012). Histopathologic effect of potassium bromate on the kidney of adult wistar rats. *Tropical Journal of Medical Research*, *16*(1), 20-23.

[4] Altoom, N. G., Ajarem, J., Allam, A. A., Maodaa, S. N., & Abdel-Maksoud, M. A. (2017). Deleterious effects of potassium bromate administration on renal and hepatic tissues of Swiss mice. *Saudi Journal of Biological Sciences*.

[5] Giridharan, R., & Sabina, E. P. (2017). Suppressive effect of Spirulina fusiformis on diclofenac-induced hepato-renal injury and gastrointestinal ulcer in Wistar albino rats: a biochemical and histological approach. *Biomedicine & Pharmacotherapy*, *88*, 11-18.

[6] Guha, M., Xu, Z. G., Tung, D., Lanting, L., & Natarajan, R. (2007). Specific down-regulation of connective tissue growth factor attenuates progression of nephropathy in mouse models of type 1 and type 2 diabetes. *The FASEB Journal*, *21*(12), 3355-3368.

[7] Humphries, S. M., Hunter, K. S., Shandas, R., Deterding, R. R., & DeBoer, E. M. (2016). Analysis of pediatric airway morphology using statistical shape modeling. *Medical & biological engineering & computing*, *54*(6), 899-911.

[8] Demir, C., & Yener, B. (2005). Automated cancer diagnosis based on histopathological images: a systematic survey. *Rensselaer Polytechnic Institute, Tech. Rep*.

[9] Sertel, O., Catalyurek, U. V., Shimada, H., & Gurcan, M. N. (2009, September). Computer-aided prognosis of neuroblastoma: Detection of mitosis and karyorrhexis cells in digitized histological images. In: *2009 Annual International Conference of the IEEE Engineering in Medicine and Biology Society*, pp. 1433-1436.

[10] Kayser, K., Radziszowski, D., Bzdyl, P., Sommer, R., & Kayser, G. (2006). Towards an automated virtual slide screening: theoretical considerations and practical experiences of automated tissue-based virtual diagnosis to be implemented in the Internet. *Diagnostic Pathology*, *1*(1), 10.

[11] Rangan, G. K., & Tesch, G. H. (2007). Quantification of renal pathology by image analysis (Methods in Renal Research). *Nephrology*, *12*(6), 553-558.

[12] Haralick, R. M., & Shapiro, L. G. (1985). Image segmentation techniques. *Computer Vision, Graphics, and Image Processing*, *29*(1), 100-132.

[13] Roy, P., Dutta, S., Dey, N., Dey, G., Chakraborty, S., & Ray, R. (2014, July). Adaptive thresholding: a comparative study. In *2014 International conference on control, Instrumentation, communication and Computational Technologies (ICCICCT)* (pp. 1182-1186). IEEE.

[14] Satapathy, S. C., Raja, N. S. M., Rajinikanth, V., Ashour, A. S., & Dey, N. (2018). Multi-level image thresholding using Otsu and chaotic bat algorithm. *Neural Computing and Applications*, *29*(12), 1285-1307.

[15] Hore, S., Chakraborty, S., Chatterjee, S., Dey, N., Ashour, A. S., Van Chung, L., & Le, D. N. (2016). An Integrated Interactive Technique for Image Segmentation using Stack based Seeded Region Growing and Thresholding. International Journal of Electrical & Computer Engineering (2088-8708), 6(6).

[16] El-Gerbed, M. S. (2014). Protective effect of lycopene on deltamethrin-induced histological and ultrastructural changes in kidney tissue of rats. *Toxicology and Industrial Health*, *30*(2), 160-173.

[17] Li, J. J., Kwak, S. J., Jung, D. S., Kim, J. J., Yoo, T. H., Ryu, D. R., Han, S.H., Choi, H. Y., Lee, J. E., Moon, S. J., Kim, D. K., Han, D. S., Kang, S.-W. (2007). Podocyte biology in diabetic nephropathy. *Kidney International*, *72*, S36-S42.

[18] Zhang, Y., Jiang, L., Jiang, L., Geng, C., Li, L., Shao, J., & Zhong, L. (2011). Possible involvement of oxidative stress in potassium bromate-induced genotoxicity in human HepG2 cells. *Chemico-biological Interactions*, *189*(3), 186-191.

[19] Succar, L., Boadle, R. A., Harris, D. C., & Rangan, G. K. (2016). Formation of tight junctions between neighboring podocytes is an early ultrastructural feature in experimental crescentic glomerulonephritis. *International journal of nephrology and renovascular disease*, 9, 297.

[20] Wright, S. I., Nowell, M. M., Lindeman, S. P., Camus, P. P., De Graef, M., & Jackson, M. A. (2015). Introduction and comparison of new EBSD post-processing methodologies. Ultramicroscopy, 159, 81-94.

[21] Shiloh, R., Remez, R., Lu, P. H., Jin, L., Lereah, Y., Tavabi, A. H., ... & Arie, A. (2018). Spherical aberration correction in a scanning transmission electron microscope using a sculpted thin film. Ultramicroscopy, 189, 46-53.

[22] Callahan, P. G., Stinville, J. C., Yao, E. R., Echlin, M. P., Titus, M. S., De Graef, M., ... & Pollock, T. M. (2018). Transmission scanning electron microscopy: Defect observations and image simulations. Ultramicroscopy, 186, 49-61.

[23] Ahmed, S. S., Dey, N., Ashour, A. S., Sifaki-Pistolla, D., Bălas-Timar, D., Balas, V. E., & Tavares, J. M. R. (2017). Effect of fuzzy partitioning in Crohn's disease classification: a neuro-fuzzy-based approach. Medical & biological engineering & computing, 55(1), 101-115.

[24] Sharma, K., & Virmani, J. (2017). A Decision Support System for Classification of Normal and Medical Renal Disease Using Ultrasound Images: A Decision Support System for Medical Renal Diseases. International Journal of Ambient Computing and Intelligence (IJACI), 8(2), 52-69.

[25] Li, Z., Shi, K., Dey, N., Ashour, A. S., Wang, D., Balas, V. E., ... & Shi, F. (2017). Rule-based back propagation neural networks for various precision rough set presented KANSEI knowledge prediction: a case study on shoe product form features extraction. Neural Computing and Applications, 28(3), 613-630.

[26] Virmani, J., Dey, N., & Kumar, V. (2016). PCA-PNN and PCA-SVM based CAD systems for breast density classification. In Applications of intelligent optimization in biology and medicine(pp. 159-180). Springer International Publishing.

[27] Hemalatha, S., & Anouncia, S. M. (2017). Unsupervised Segmentation of Remote Sensing Images using FD Based Texture Analysis Model and ISODATA. International Journal of Ambient Computing and Intelligence (IJACI), 8(3), 58-75.